J. Meas. Sci. Instrum., 2024, 15(1): 105-119.
DOI: 10.62756/jmsi.1674-8042.2024011
http://jmsi.publish.founderss.cn/
jmsi@nuc.edu.cn

A testing platform for frequency response characteristics of linear Hall sensors

LIU Yu[1], HU Liangliang[2,3*], LIAO Mingzhao[4], ZHOU Ru[1], XU Jinzhang[1]

1. School of Electrical Engineering and Automation, Hefei University of Technology, Hefei 230009, China;
2. School of Instrument Science and Optoelectronics Engineering, Hefei University of Technology, Hefei 230009, China;
3. Anhui Province Key Laboratory of Measuring Theory and Precision Instrument, Hefei University of Technology, Hefei 230009, China;
4. School of Microelectronics, Hefei University of Technology, Hefei 230601, China

***Corresponding author:** HU Liangliang (friendyhu@hfut.edu.cn)

Received: January 5, 2024 **Revised:** March 11, 2024 **Accepted:** March 16, 2024

Abstract: Linear Hall sensors are widely used to measure magnetic field strength, but there are few studies on the dynamic response characteristics of Hall sensors. To tackle this issue, a testing platform for the frequency response characteristics of linear Hall sensors was built, which was composed of a controllable constant current source, coils, linear Hall sensors, a low noise amplifier, and a data acquisition device. The system transfer function was constructed and a method of dynamically updating the transfer function was proposed, which realizes the accurate measurement of the dynamic response characteristics of Hall sensors. The dynamic characteristics of NHE520F and P3A were tested on this platform. The results showed that the performance differences in amplitude-frequency and phase-frequency characteristics of these Hall sensors in the range of 2.5 kHz — 2 MHz were fully reflected on this testing platform. The dynamic characteristic parameters of Hall sensors were not necessarily consistent with the static characteristic parameters of Hall sensors, and the distributions of dynamic characteristics were also different. Additionally, according to the amplitude-frequency and phase-frequency characteristics of Hall sensors measured under various temperature and humidity conditions, the average dynamic characteristic curves and three standard deviation envelope curves of Hall sensors were plotted. The data obtained by this testing platform are of great significance for the research of dynamic response characteristics of Hall sensors.

Key words: Hall sensor; magnetic field measurement; amplitude-frequency characteristics; phase-frequency characteristics

0 Introduction

The Hall elements are sensors based on Hall effect, specifically designed for detecting magnetic field strength, direction, and position as well as measuring electric current magnitude and speed[1]. These elements possess characteristics of compactness, low power consumption, high precision, and high reliability that render them extensively applicable across diverse domains encompassing scientific research to industrial production[2,3]. Their inherent advantages in terms of small form factor, minimal energy requirements, and high accuracy establish their indispensability within numerous contemporary technologies and devices. Therefore, research on Hall elements and Hall effect has been continuously advancing to meet the diverse demands of various fields. In power systems, Hall element-based current transformers are employed for circuit metering and fault protection[4,5]. A Hall-effect current transformer using automatic DC bias calibration method has been applied to power system. The current transformer using this method can eliminate Hall-IC DC bias voltage and adopt digital filter to filter noise to obtain better accuracy[6]. In microelectronics, highly precise Hall elements facilitate the development of micro devices as well as microelectronic systems[7]. For example, a Hall sensor, as an integrated power measurement system of a paranoid circuit, has been widely used in the field of microelectronics[8]. Due to the high sensitivity requirements of Hall sensors in the field of microelectronics, Hall sensors are also constantly developing to adapt to different needs, and bismuth-based Hall sensors have been developed, which have a broad future in the field of microelectronics[9]. Moreover, owing to advancements in sensor technology, Hall elements are frequently utilized as versatile sensors capable of measuring magnetic fields, temperatures[10,11], and other parameters to cater to a wide range of applications. For example, in the field of power system, the current transformer based on Hall effect is also developing towards multi-function: not only can distinguish load

current and fault current, but also has the function of measurement and protection, thereby improving the accuracy and precision of power current measurement[12].

Current research on Hall elements primarily focuses on their static characteristics and applications, while ongoing efforts also explore the dynamic response characteristics of these elements. The latter refers to how Hall elements behave and perform under changing input or operating conditions, encompassing factors such as response time, stability, temperature sensitivity, noise characteristic, sensitivity range and frequency. The testing platform designed in this work is specifically for the amplitude-frequency and phase-frequency characteristics of Hall sensors because these characteristics play a crucial role in their performance evaluation. Firstly, comprehending the response characteristics of Hall elements at different frequencies enables optimization of their design for enhanced sensor performance across diverse applications. Secondly, understanding the amplitude-frequency characteristics of Hall sensors facilitates determination of their applicable frequency range, thereby expanding their potential utilization in various fields such as high-speed rotating equipment speed detection[13], AC current measurement, etc. In high-frequency environments, the interference of noise on Hall sensors has emerged as a significant concern. By investigating the amplitude-frequency characteristics, one can enhance the design of filters and other circuits to mitigate or eliminate the impact of noise. The frequency response of Hall sensors may influence the stability and performance of entire systems in certain cases. A comprehensive exploration into these characteristics can facilitate the development of more stable and reliable systems. Moreover, an in-depth study on Hall sensor′s amplitude-frequency characteristics holds potential for advancing technologies by enabling their adaptation to a wider frequency range with heightened sensitivity[14,15]. Therefore, it is crucial to accurately measure the dynamic response characteristics of Hall sensors. Investigating the phase-frequency characteristics of Hall sensors enables analysis of their response to input signals at varying frequencies. Understanding the system′s phase characteristics across different frequencies aids in determining its dynamic performance, encompassing both response speed and phase delay[16]. In certain applications, specific requirements exist for the response time and phase delay of Hall sensors. By analyzing the phase-frequency characteristics, it becomes possible to design within the frequency domain to meet the performance demands of a particular application[17].

Therefore, we designed a testing platform to measure the dynamic response characteristics of Hall sensors. The testing methodology comprises two parts: an independent performance test and data calculation. The independent performance test divides the platform into several modules including a constant-current source module, a coil module, a low-noise amplifier, and a data processing module to individually test their dynamic response characteristics as well as that of the entire platform. According to the relationship between the dynamic response characteristics of each module and the dynamic response characteristics of the platform, the dynamic response characteristics of Hall sensor can be obtained by mathematical calculation. By this method, interference factors in the testing platform can be accurately stripped out, so that the dynamic response characteristics of Hall components can be obtained. Furthermore, the temperature and humidity experiments on the testing platform were carried out to judge the stability of the testing platform under different temperature and humidity environments.

1 Basic theory

Hall element is a type of sensor that detects magnetic fields based on Hall effect. Its working principle is illustrated in Fig.1.

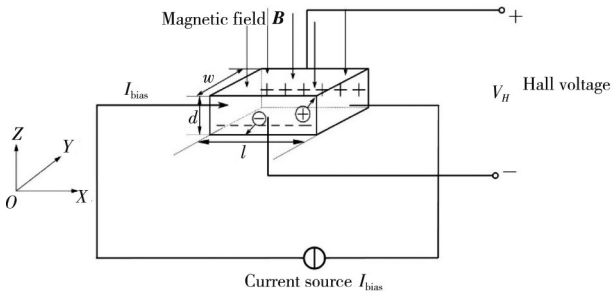

Fig. 1 Working principle diagram of Hall element

When a current I_{bias} passes through the semiconductor in the presence of a magnetic field B, charged particles within the semiconductor experience the Lorentz force. Negative electrons move in the negative direction along the Y-axis, while positive electrons move in the positive direction along the Y-axis. Eventually, they accumulate at both edges of the semiconductor along its Y-axis, forming an electric field E. This electric field E generates an opposing force to counteract the Lorentz force. As more and more electrons migrate, both electric field strength E and electric field force increase accordingly until they reach equilibrium with the Lorentz force. At this point, electron deflection ceases and electric field E stabilizes. The potential difference V_H across

both ends of the semiconductor remains constant[15]. Thus, the corresponding Hall voltage calculation formula can be derived as

$$V_{\mathrm{H}} = R_{\mathrm{h}} \frac{I_{\mathrm{bias}} B}{d}, \tag{1}$$

where V_{H} is the Hall voltage, R_{h} is the Hall coefficient, I_{bias} is the current flowing through the Hall sensor, B is the magnetic flux density, and d is the thickness of the Hall sensor. Due to its susceptibility to interference and low signal strength, an amplifier circuit is essential at the output stage of the Hall sensor. In the testing platform, Hall sensor is powered by 12 V power adapter with 5 mA current regulative diode.

The testing platform for Hall sensors consists of a signal generator, a constant current source, a coil for magnetic field generation, the Hall effect sensor under test, a power supply circuit for the sensor, a low noise amplifier, and a data acquisition device. The stanford research systems model DS345 30 MHz synthesized function generator was utilized as the signal generator in this platform. This instrument is commonly employed for generating diverse waveform signals to facilitate testing as well as research and development activities. Sine wave signals ranging from 2.5 kHz to 2 MHz are available on this platform. A constant current source refers to an element or a module within an electrical circuit that provides a stable current output, unaffected by load variations and power supply fluctuations. It plays a crucial role in generating an alternating magnetic field in the test rig. The testing platform utilizes a constant current source based on the OPA541 operational amplifier[18]. The Hall sensors under test are NHE520F-6, NHE520F-7, NHE520F-8 and P3A. Due to the small output V_{H} of the Hall sensor during operation, which hampers direct observation and is susceptible to noise interference, direct measurement of the dynamic response characteristics of the Hall sensor becomes impractical. Hence, an output-end low-noise amplifier was employed to address these challenges[19]. The low-noise amplifier (LNA) could provide a 30 dB gain for amplifying the Hall output voltage from the Hall sensor[20]. The amplified signal was then observed through an A/D module and subsequently transmitted via a microprogram controller (MCU) and local area network (LAN) for data calculation on a computer. Fig.2 illustrates the testing platform.

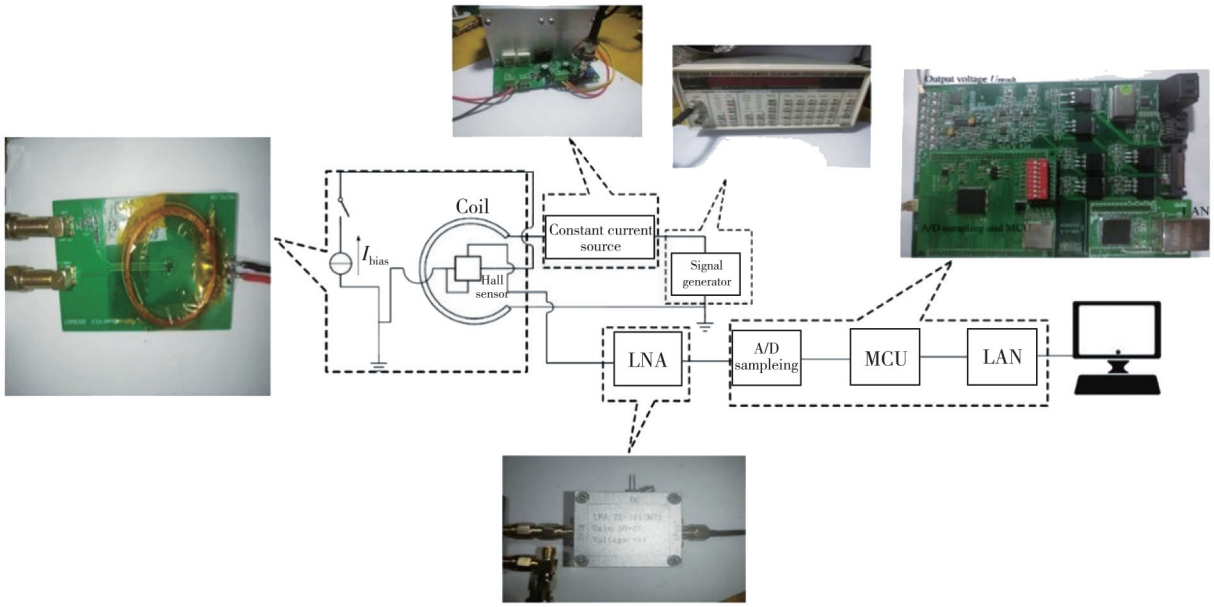

Fig. 2 Hall sensor performance testing platform

In the test rig, the signal generated from the signal generator passes through a constant current source, a coil, a Hall effect sensor, and a low noise amplifier in turn, and then it elicits a distinct dynamic response characteristic in each module. Consequently, the observed response characteristic of the Hall sensor is an outcome of the combined influence of these individual module responses. To determine the dynamic response characteristics of the Hall sensor, it becomes imperative to acquire transfer functions for every module's dynamic response characteristics. Subsequently, by leveraging mathematical relationships between the transfer functions of each module and the transfer function of entire testing platform, and isolating the dynamic response characteristics of each module from entire testing platform's dynamic response characteristics through calculation, the dynamic response characteristics of Hall sensors can be obtained. Here, the frequency response transfer functions of all modules are set as H_1 , H_2, H_3 and H_{result}, respectively, and they are

decomposed into amplitude-frequency characteristic $A(\omega)$ and phase-frequency characteristic $\varphi(\omega)$ by

$$H(\omega)=A(\omega)e^{j\varphi(\omega)}. \tag{2}$$

The transfer function partition diagram is shown in Fig.3.

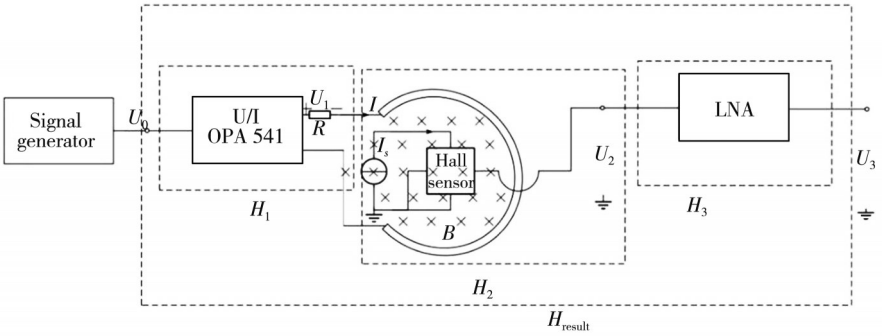

Fig. 3 Transfer function partition diagram

The relationship of transfer functions of all modules, the relationship of phase-frequency characteristics of all modules, and the amplitude-frequency characteristics of all the modules are expressed respectively as

$$NH_1(\omega)H_2(\omega)H_3(\omega)=H_{result}(\omega), \tag{3}$$

$$\varphi_1(\omega)+\varphi_2(\omega)+\varphi_3(\omega)=\varphi_{result}(\omega), \tag{4}$$

$$NA_1(\omega)A_2(\omega)A_3(\omega)=A_{result}(\omega), \tag{5}$$

where H_1 is the transfer function of constant current source; H_2 is the transfer function of Hall sensor, and it is also the dynamic response characteristic of Hall sensor; H_3 is the transfer function of low noise amplifier; H_{result} is the transfer function of the testing platform; φ_1 is the phase-frequency characteristic of constant current source; φ_2 is the phase-frequency characteristic of Hall sensor; φ_3 is the phase-frequency characteristic of low noise amplifier; and φ_{result} is the phase-frequency characteristic of the testing platform; A_1 is the amplitude-frequency characteristic of constant current source; A_2 is the amplitude-frequency characteristic of Hall sensor; A_3 is the amplitude-frequency characteristic of low noise amplifier; A_{result} is the amplitude-frequency characteristic of the testing platform; and N is the number of turns of a coil that produces an alternating magnetic field. The amplitude-frequency characteristic of Hall sensor is shown as

$$A_2=\frac{|A_{result}|}{|A_1||A_3|N}, \tag{6}$$

and the phase-frequency characteristic of Hall sensor is shown as

$$\varphi_2=\varphi_{result}-\varphi_1-\varphi_3. \tag{7}$$

The dynamic response characteristics of the Hall sensor can be obtained by measuring A_1, A_2, A_{result}, φ_1, φ_3 and φ_{result} and then calculating them by the above equations. In the process of measuring A_1, A_2 and A_{result}, to obtain accurate measured data, it is imperative to meticulously process the collected signal at each frequency, employ a Hilbert transform on the acquired signal for every frequency by

$$\hat{U}_n(t)=\frac{1}{\pi}\int_{-\infty}^{+\infty}\frac{U(\tau)}{t_n-\tau}d\tau, \tag{8}$$

and follow signal analysis by

$$\tilde{U}_n(t)=U_n(t)+j\hat{U}_n(t). \tag{9}$$

In Eq. (9), the real part is the output signal and the imaginary part is the Hilbert transform of the output signal. Based on the Hilbert transform, we can get

$$\left|\tilde{U}_n(t_r)\right|=\sqrt{U_n{}^2(t_r)+\hat{U}_n{}^2(t_r)}=|U_n|, \tag{10}$$

where $|U_n|$ is the amplitude of the output signal at any moment $t_r(r=0,1,\cdots,n)$.

Subsequently, the signals each every frequency are collected as $U_0(t_0)$, $U_1(t_1)$, $\cdots$, $U_n(t_n)$, and then $\hat{U}_0(t_0)$, $\hat{U}_1(t_1),\cdots,\hat{U}_n(t_n)$ can be obtained by Eq. (8). Substituting the above values into Eqs. (9) and (10), respectively, $\tilde{U}_0(t_0),\tilde{U}_1(t_1),\cdots,\tilde{U}_n(t_n)$ and $|U_1|,|U_2|,\cdots,|U_n|$ can be obtained correspondingly.

The amplitude-frequency characteristics at each frequency can be obtained

$$A_n=\frac{|U_n|}{|U_{in}|}, \tag{11}$$

where $|U_{in}|$ is the amplitude of the input signal.

2 Experiment

By testing the dynamic response characteristics of the Hall element, the performance of the testing platform can be reflected. In this work, the testing platform was split into a sensor module, a constant current source module and an LNA module, where the sensor module is shown in Fig.4(a) and the actual Hall sensor is shown in Fig. 4(b). The sensor module can be obtained by coupling the coil in the constant current source module with the sensor and its power supply circuit via a

magnetic field. Since the Hall voltage is proportional to the current size and the number of coil turns N, its transfer function is expressed as

$$H_2(\omega)=\frac{U_2}{I}=\left|A_2(\omega)\right|e^{j\varphi_2(\omega)}. \tag{12}$$

Eq. (12) is also the dynamic response characteristics of a Hall sensor.

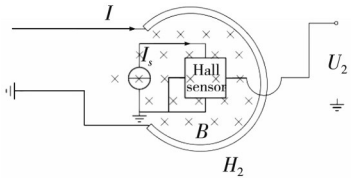

(a) Diagram of Hall sensor module

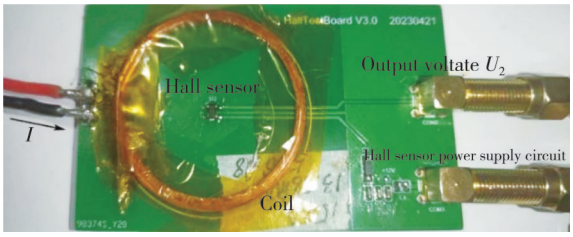

(b) Actual Hall sensor

Fig. 4 Hall sensor module

In our work, the following experiments were conducted to obtain the dynamic response characteristics of the Hall sensor:

Experiment 1: Measuring the transfer function H_1 of the constant current source.

The transfer function of the constant current source is expressed as

$$H_1(\omega)=\frac{I}{U_0}=\left|A_1(\omega)\right|e^{j\varphi_1(\omega)}. \tag{13}$$

The schematic diagram of the constant current source module is depicted in Fig. 5 (a), and the actual constant current source is shown in Fig. 5 (b).

To measure the amplitude-frequency characteristic $A_1(\omega)$ of the constant-current source module, a sampling resistor R was connected in series with the coil winding during the experiment. Additionally, an A/D module was connected in parallel with resistor R to measure U_1. The amplitude-frequency characteristic was calculate by

$$A_1(\omega)=\frac{IR}{U_0R}=\frac{U_1(\omega)}{U_0R}. \tag{14}$$

Then, the phase difference φ_1 between U_0 and U_1 was measured, as shown in Fig. 5 (c), and the voltage U_1 across both ends of the sampling resistor within a frequency range of 2.5 kHz—2 MHz was measured. The steps for calculating the amplitude-frequency and phase-frequency characteristics of a constant current source module are as follows:

1) Collecting the output signal (U_1) of each frequency using the A/D sampling module.

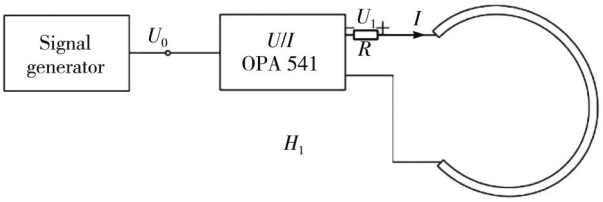

(a) Schematic diagram of constant current source module

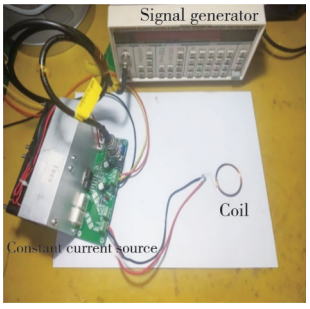

(b) Actual constant current source

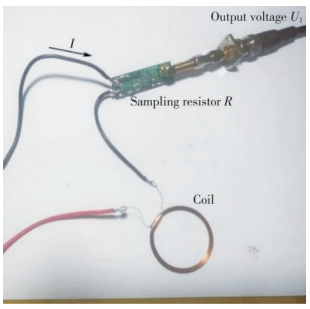

(c) Sampling resistance R

Fig. 5 Constant current module and sampling method

2) Transmitting the output signal to the MCU, performing Hilbert transformation on the module by Eq. (8), and analyzing the output signal by Eq. (9).

3) Calculating the amplitude of the output signal at every frequency by Eq. (10), calculating the amplitude-frequency characteristics of the output signal at every frequency by Eq. (11), and measuring the phase difference φ_1 between U_0 and U_1 at every frequency.

4) Storing the amplitude-frequency characteristics of output signal at every frequency and the phase difference between the output signal and the input signal in the RAM register of MCU.

5) Plotting the results above on the computer and obtaining the amplitude-frequency characteristic curve $A_1(\omega)$ and phase-frequency characteristic curve $\varphi_1(\omega)$.

Experiment 2: Measuring the transfer function of the low-noise amplifier H_3.

The transfer function of the low-noise amplifier is expressed as

$$H_3=\frac{U_3}{U_2}=\left|A_3(\omega)\right|e^{j\varphi_3(\omega)}. \tag{15}$$

The schematic diagram of the low-noise amplifier module is shown in Fig. 6 (a), and the actual low-noise amplifier is shown in Fig. 6 (b).

The steps for measuring the transfer function of the LNA within a frequency range of 2.5 kHz—2 MHz are as follows:

1) Collecting the output signal U_3 of every frequency using the A/D sampling module.

2) Transmitting the output signal to the MCU module for Hilbert transformation by Eq. (8), and then analyzing

the output signal by Eq. (9).

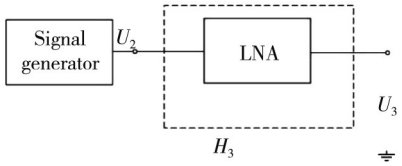

(a) Schematic diagram of low-noise amplifier module

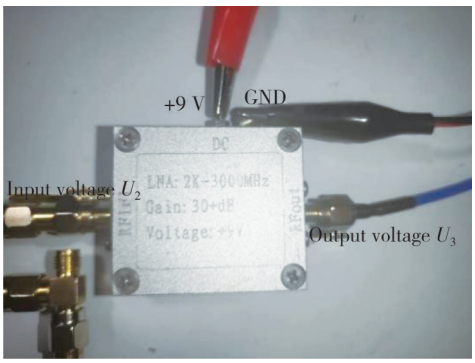

(b) Actual low-noise amplifier

Fig. 6 Low-noise amplifier

3) Calculating the amplitude of the output signal at every frequency by Eq. (10), calculating the amplitude-frequency characteristic of the output signal at every frequency by Eq. (11), and measuring the phase difference φ_3 between U_2 and U_3 at every frequency.

4) Storing the amplitude-frequency characteristics of the output signal at every frequency and the phase difference between the output signal and the input signal in the RAM register of MCU.

5) Plotting the results above on the computer and obtaining the amplitude-frequency characteristic curve $A_3(\omega)$ and phase-frequency characteristic curve $\varphi_3(\omega)$

Experiment 3: Measuring the dynamic response characteristics of the platform.

Loading NHE520F-6, NHE520F-7, NHE520F-8 and P3A into the testing platform successively to measure the dynamic response characteristics of the testing platform under the above three Hall sensors. The transfer function within the frequency range of 2.5 kHz—2 MHz can be calculated by

$$H_{\text{result}} = \frac{U_3}{U_0} = \left| A_{\text{result}}(\omega) \right| e^{j\varphi_{\text{result}}(\omega)}. \tag{16}$$

The steps for measuring the transfer function within a frequency range of 2.5 kHz—2 MHz are as follows:

1) Collecting the output signal (U_{result}) of every frequency using the A/D sampling module.

2) Transmitting the output signal to the MCU module for Hilbert transformation by Eq. (8), and analyzing the output signal by Eq. (9).

3) Calculating the amplitude of the output signal at every frequency by Eq. (10), calculating the amplitude-frequency characteristics of the output signal at every frequency by Eq. (11), and measuring the phase difference φ_{result} between U_0 and U_3 at every frequency.

4) Storing the amplitude-frequency characteristics of the output signal at every frequency and the phase difference between the output signal and the input signal in the RAM register of MCU.

5) Plotting the data above on the computer and obtaining the amplitude-frequency characteristic curve $A_{\text{result}}(\omega)$ and phase-frequency characteristic curve $\varphi_{\text{result}}(\omega)$.

After conducting the aforementioned experiments, the amplitude-frequency characteristic $A_1(\omega)$, $A_3(\omega)$ and $A_{\text{result}}(\omega)$, as well as the phase-frequency characteristic $\varphi_1(\omega)$, $\varphi_3(\omega)$ and $\varphi_{\text{result}}(\omega)$ have been stored in the RAM register of MCU. Consequently, the data stored in RAM can be accessed by the MCU module for calculation purposes. The MCU module calculates the amplitude-frequency characteristic $A_2(\omega)$ of the Hall sensor by Eq. (6) and determines its phase-frequency characteristic $\varphi_2(\omega)$ by Eq. (7). Then $A_2(\omega)$ curve and $\varphi_2(\omega)$ curve are drawn on the computer.

Finally, the characteristics of the testing platform at different temperature and in different humidity environments were tested. Firstly, the constant current source module and LNA module were placed in the constant temperature and humidity test chamber, and the sensor module was placed outside the thermostat. The amplitude-frequency and phase-frequency characteristics of the Hall sensors were tested at 15 ℃ 50%Rh, 15 ℃ 60%Rh, 15 ℃ 70%Rh, 25 ℃ 50%Rh, 25 ℃ 60%Rh, 25 ℃ 70%Rh, 35 ℃ 50%Rh, 35 ℃ 60%Rh and 35 ℃ 70%Rh, respectively. Secondly, different temperature and humidity data tested at every frequency were averaged as the reference base. Thirdly, the standard deviation of these tested data were calculated. At last, the consistency of the tested data of the platform was evaluated based on the probability greater than 99.7% within 3 standard deviations.

3 Experimental results

The amplitude-frequency characteristic A_1 of the constant-current source module and the amplitude-frequency characteristic A_3 of the LNA are obtained based on the experimental procedures described in the previous section, as illustrated in Fig.7 (a) and (b). It is evident that the output current of the constant current source decreases with increasing frequency, and the LNA can provide stable amplification gain in the high frequency range, as shown in Fig.7.

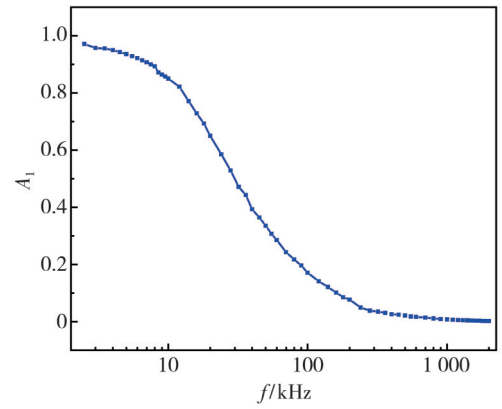

(a) Amplitude-frequency characteristic A_1 of constant current source module

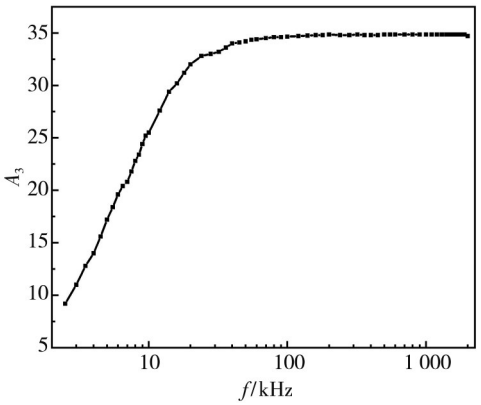

(b) Amplitude-frequency characteristic A_3 of low noise amplifier

Fig. 7 Amplitude-frequency characteristics of constant current source and LNA

The amplitude-frequency characteristics of experimental platform are measured as depicted in Fig.8(a), followed by calculation of Hall sensor′s amplitude-frequency characteristics by Eq. (6), as shown in Fig. 8(b). It is evident that the maximum Hall output voltage of the three Hall sensors occurs at 280 kHz. Moreover, within the frequency range of 2.5 kHz—280 kHz, the Hall voltage exhibits an increasing trend with rising frequency, while within the range of 280 kHz—1.5 MHz, it demonstrates a decreasing trend with increasing frequency. Within the frequency range of 2.5 kHz—18 kHz, the Hall voltage of P3A exhibits a decreasing trend with rising frequency, while within the range of 18 kHz—2 MHz, it demonstrates an increasing trend with increasing frequency. It can be clearly illustrated that NHE520F exhibits favorable amplitude-frequency characteristics within 20 kHz — 1 MHz. Additionally, in Fig. 8(b), when the testing frequency is in the range of 2.5 kHz — 38 kHz, the sensitivity values of the three NHE520F Hall sensors are arranged from high to low as NHE520F-8, NHE520F-7 and NHE520F-6 in turn. This order is consistent with the order of their sensitivity values in a static environment. When the testing frequency is in the 38 kHz—2 MHz range, the sensitivity values of the three Hall sensors are arranged from high to low as NHE520F-8, NHE520F-6 and NHE520F-7 in turn. Within the frequency range of 2.5 kHz—2 MHz, the sensitivity of Hall sensor P3A is lower than that of NHE520F.

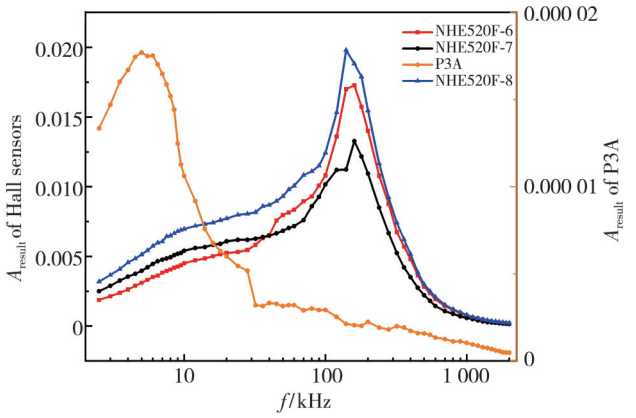

(a) Amplitude-frequency characteristic of sensors test platform ignoring the effect of system transfer function

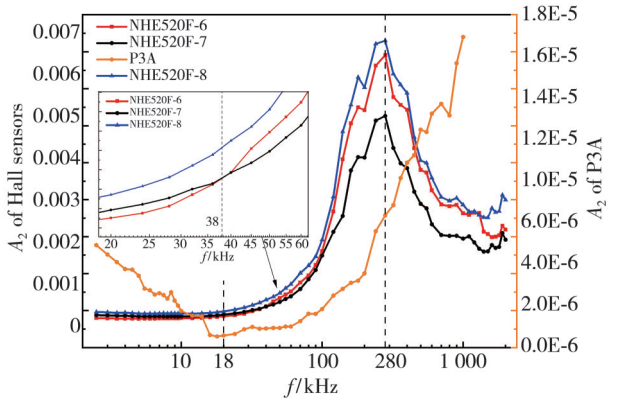

(b) Amplitude-frequency characteristic of Hall sensors

Fig. 8 Amplitude-frequency characteristics of entire testing platfom and Hall sensors

It can be seen from Fig. 9 that in terms of the phase-frequency characteristic φ_1 of the constant current source module in the frequency range of 2.5 kHz—2 MHz and the phase-frequency characteristic φ_3 of the LNA, there is an increasing phase difference between the input voltage of constant current source and the current that generates the alternating magnetic field as the frequency increases, and the phase of the current that generates an alternating magnetic field precedes the phase of the input voltage of constant current source. The output voltage phase of the LNA exhibits a lag behind the input voltage phase within the frequency range of 2.5 kHz—240 kHz, as depicted in Fig. 9(b), whereas it demonstrates a lead over the input voltage phase within the frequency range of 240 kHz—2 MHz.

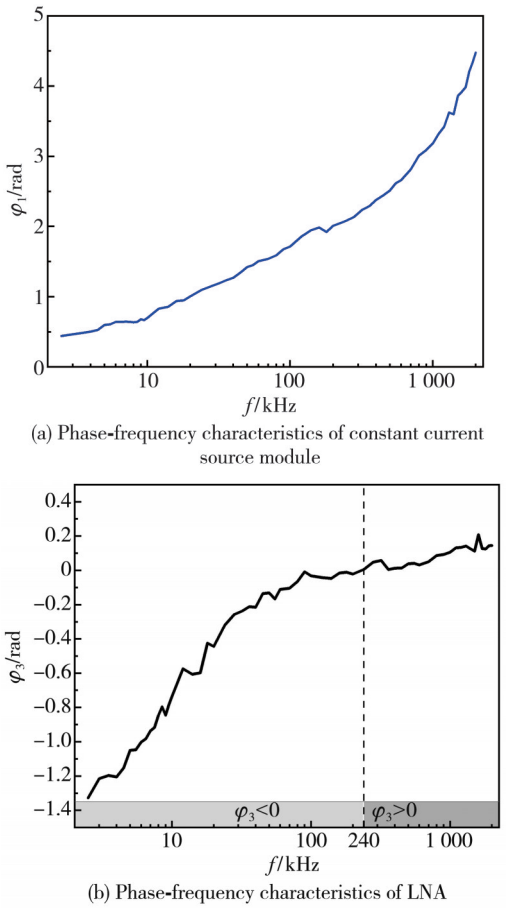

Fig. 9 Phase-frequency characteristics of constant current source and LNA

The phase-frequency characteristics of the entire testing platform are illustrated in Fig.10.

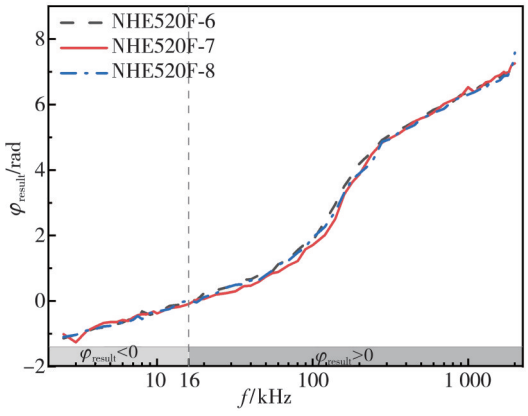

Fig. 10 Phase-frequency characteristics of the platform (NHE520F)

It can be seen that the output voltage exhibits a phase lag relative to the input voltage within the frequency range of 2.5 kHz—16 kHz, while in the frequency range of 16 kHz—2 MHz, and the phase of the output voltage is ahead of the phase of the input voltage. The phase-frequency characteristics for the three Hall sensors can be calculated by Eq. (7) and presented in Fig. 11(a), (b) and (c), respectively. In the range of 2.5 kHz—80 kHz, the phase of the output voltage of NHE520F-6 lags behind the phase of the current that generates the alternating magnetic field, and the phase of the output voltage of NHE520F-6 is ahead of the phase of the current that generates the alternating magnetic field in the range of 80 kHz—2 MHz, as sjown in Fig.11(a).

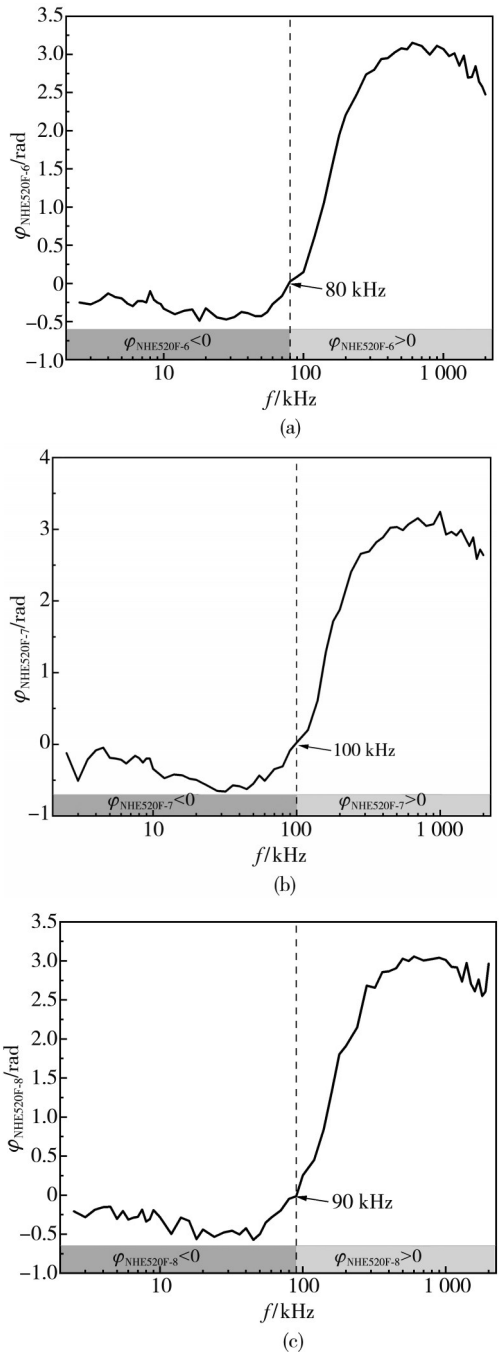

Fig. 11 Phase-frequency charactoristics of NHE520F

In the range of 2.5 kHz—100 kHz, the phase of the output voltage of NHE520F-7 lags behind the phase of the current that generates the alternating magnetic field, and the phase of the output voltage of NHE520F-7 is ahead of the phase of the current that generates the alternating magnetic field in the range of 100 kHz—2 MHz, as shown

in Fig.11 (b).

In the range of 2.5 kHz—90 kHz, the phase of the output voltage of NHE520F-8 lags behind the phase of the current that generates the alternatingmagnetic field, and the phase of the output voltage of NHE520F-8 is ahead of the phase of the current that generates the alternating magnetic field in the range of 90 kHz—2 MHz , as shown in Fig.11 (c).

By loading the P3A into the experimental platform, measuring the phase frequency characteristics of the entire experimental platform, and calculating the phase frequency characteristic of P3A by Eq. (7), we can get the phase-frequency characteristics of the platform (P3A) and phase-frequency characteristic of P3A, as shown in the Fig.12.

The phase - frequency characteristic of the entire experimental platform is illustrated in Fig.12. The output voltage exhibits a phase lag relative to the input voltage within the frequency range of 2.5kHz—7.5kHz, while in the frequency range of 7.5kHz—2MHz, the phase of the output voltage is ahead of the phase of the input voltage. Within the frequency range of 2.5 kHz—2 MHz, only in the range of 6 kHz—36 kHz, the phase of Hall voltage of P3A leads ahead of the current that generates the alternating magnetic field.

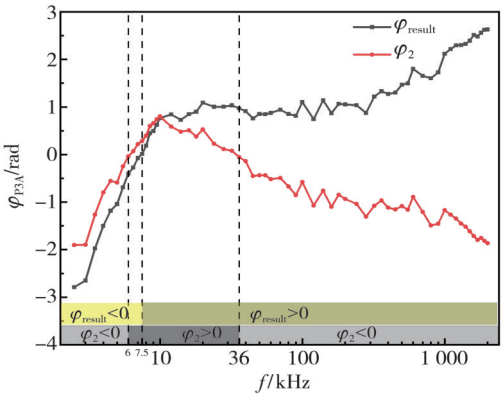

Fig. 12 Phase-requency characteristics of the platform (P3A) and phase-frequency characteristics of P3A

Temperature and humidity environmental testing data are displayed as tested data part and statistical data part, respectively. Each part contains amplitude-frequency characteristics and phase-frequency characteristics, and there are four charts totally. Fig.13 shows the amplitude-frequency characteristics of Hall sensors under different temperature and humidity environments.

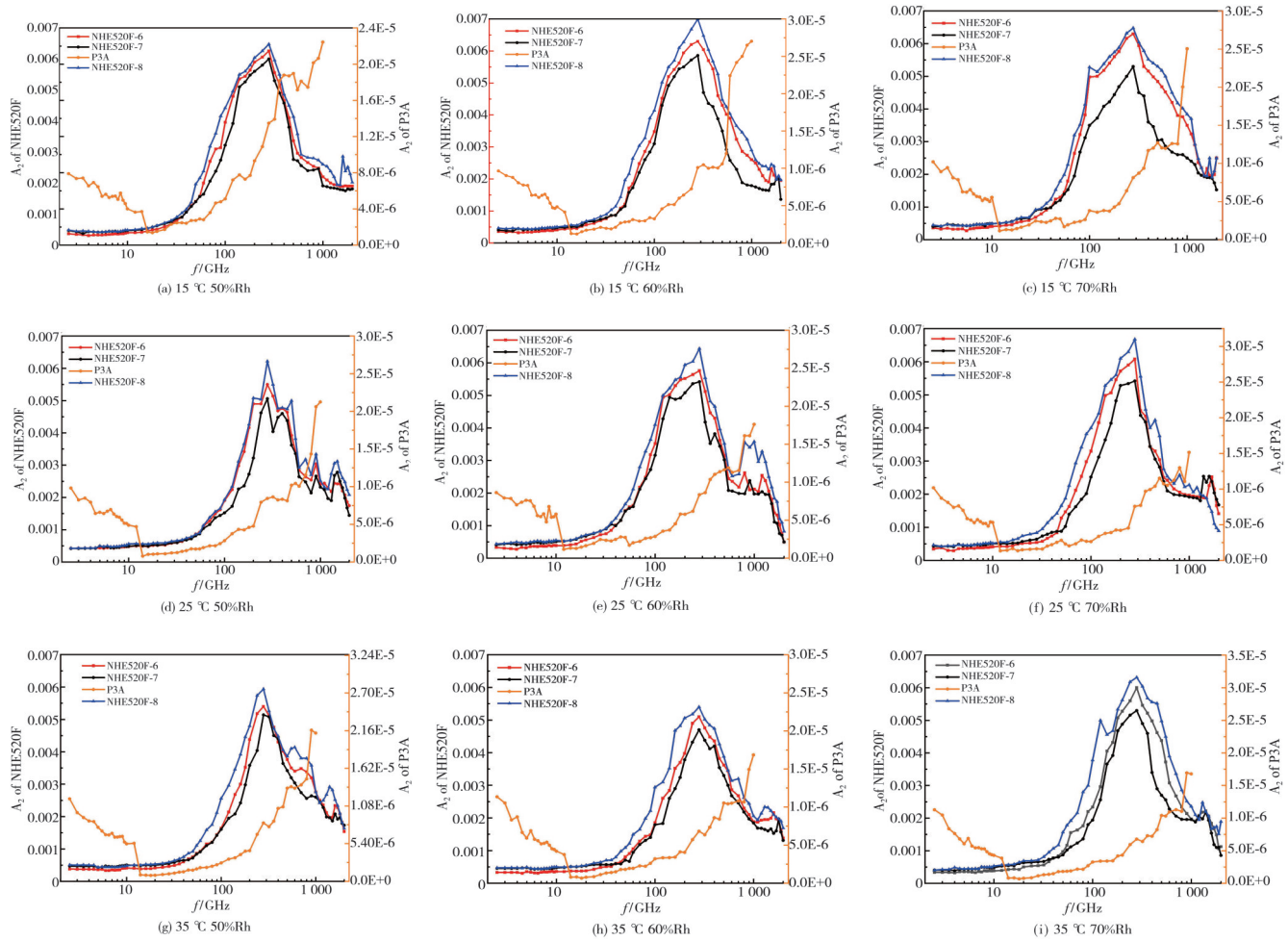

Fig. 13 Amplitude-frequency characteristics of Hall sensors at different temperatures and in different humidity environments

It is divided into 9 subgraphs, each of which contains the amplitude-frequency characteristics curves of NHE520F-6, NHE520F-7, NHE520F-8 and P3A. The lines marked with blue triangles represent NHE520F-8, the lines marked with black circles represent NHE520F-7, the lines marked with red squares represent NHE520F-6, and the lines marked with orange diamonds represent P3A. In the horizontal direction, from left to right, the temperature remains unchanged, and the humidity parameter gradually increases. In the vertical direction, from top to bottom, the humidity remains the same and the temperature gradually increases.

Fig. 14 is the statistical analysis diagram of Hall sensors' amplitude-frequency characteristics, which contains four subgraphs, namely NHE520F-6, NHE520F-7, NHE520F-8 and P3A. The lines marked by black squares are average curves, and the lines marked by red dots are curves of positive 3 standard deviations. The line marked by the blue triangle is a curve of negative 3 standard deviations. The gray areas are the floating areas of Hall sensors' amplitude-frequency characteristics.

Fig. 15 shows the phase-frequency characteristics of hall sensors under different temperature and humidity environments. It includes 9 subgraphs, each of which contains the phase frequency characteristic curves of NHE520F-6, NHE520F-7, NHE520F-8 and P3A, where the lines marked with blue triangles represent NHE520F-8, the lines marked with black circles represent NHE520F-7, the lines marked with red squares represent NHE520F-6, and the lines marked with orange triangles represent P3A. In the horizontal direction, from left to right, the temperature remains unchanged, and the humidity parameter gradually increases. In the vertical direction, from top to bottom, the humidity remains the same and the temperature gradually increases.

Fig. 16 is the statistical analysis diagram of the phase frequency characteristics of Hall sensors, which contains four subgraphs, namely NHE520F-6, NHE520F-7, NHE520F-8 and P3A, where the lines marked by the black square are the mean curve, and the lines marked by the red dot are the curves of positive 3 standard deviations. The line marked by the blue triangle is a curve of negative 3 standard deviations. The gray areas are the floating areas of the phase frequency characteristics of the Hall sensors.

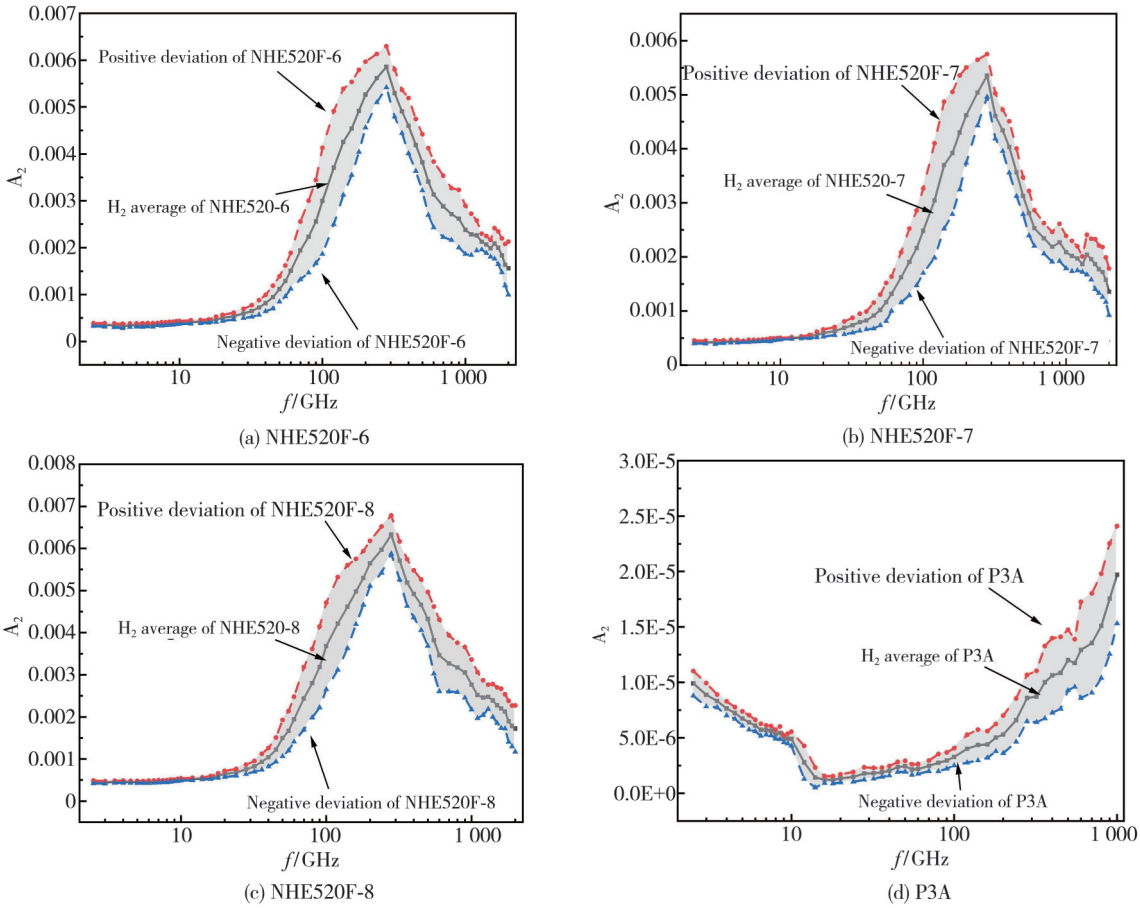

Fig. 14 Statistical analysis diagram of Hall sensors' amplitude-frequency characteristics

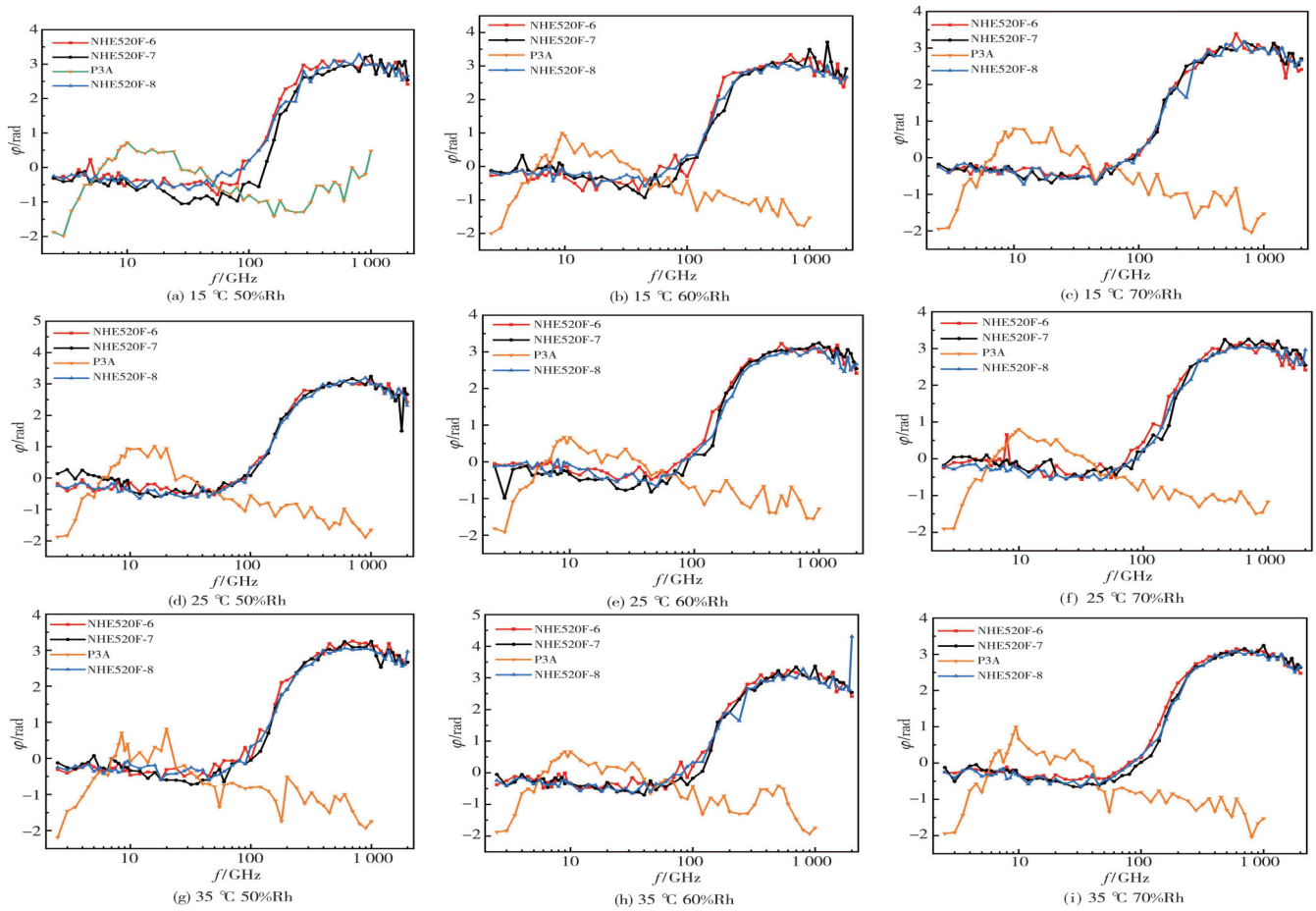

Fig. 15 Phase-frequency characteristics of Hall sensors in different temperature and humidity environments

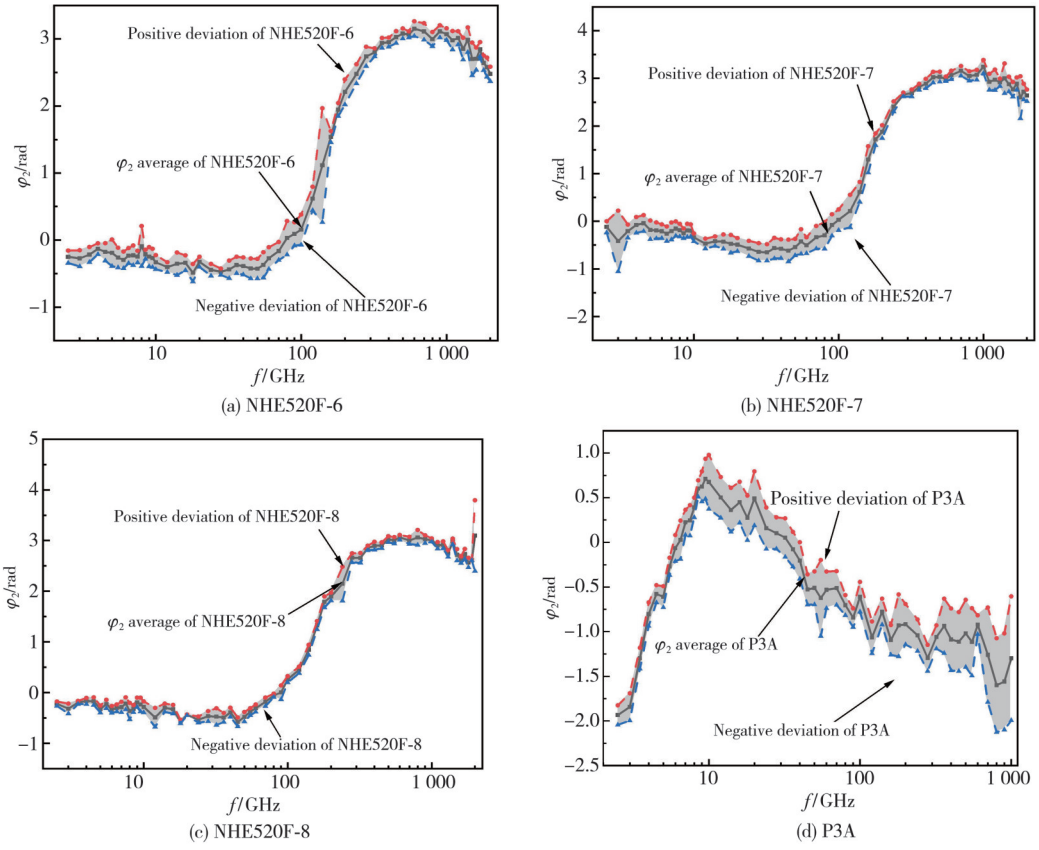

Fig. 16 Statistical analysis diagram of Hall sensors´ phase-frequency characteristics

4 Discussion

The designed testing platform presents the transfer functions of all the core components, provides the measurement methods for all transfer functions, and deduces the mathematical relationship between them. On the testing platform, the amplitude-frequency characteristics (Fig. 8(b)) and phase-frequency characteristics (Fig. 11) of three static sensitivity parameters of NHE520F were tested. The following section will discuss the problems encountered during the testing process, propose improvement measures, and analyze and evaluate the effectiveness of the constructed platform.

The presence of noise significantly influences the accuracy of measurements. Switch-mode power supplies and power grid systems generate numerous interference signals. These signals can cause substantial deviations in tested data at specific frequency points. Introducing appropriate filtering measures, isolation measures, and battery-powered measures contributes to reducing system noise and minimizing measurement errors.

Coils are essential for the magnetic field generator. The Hall voltage output by the Hall sensor is proportional to the current in the coil, and the Hall voltage output by the Hall sensor is also proportional to the number of turns in the coil. Increasing the number of turns of the coil can improve the magnetic field strength, but there is a resonant loop between the parasitic capacitor and the coil itself, and the resonant current does not pass through the measurement resistance. Too many turns of the coil will make the resonant frequency of the coil fall within the range of the testing frequency, thus affecting the accuracy of the experiment. Therefore, the experiment should avoid resonance as much as possible. We carried out two additional experiments using 5-turn and 1-turn coils, respectively. The experimental results are consistent. Therefore, to avoid coil resonance during the experiment, we used a 1-turn coil to measure the NHE520F series Hall sensor. The sensitivity of Hall sensor P3A is low, the experiment uses a 100-turn coil,

while increasing the current intensity. The experimental results do not produce a peak. Therefore, it can be determined that the resonant point of the coil must be above 2 MHz, the peak of the NHE520F series must not be the resonance characteristics of the coil, and the peak of the NHE520F series reflects the characteristics of the device itself. Fig. 8(b) shows the amplitude-frequency characteristics of Hall devices of NHE520F and P3A. The amplitude-frequency characteristics of Hall sensors, which are directly measured by the testing platform, can be seen in Fig. 8(a). It is evident that an increase in frequency within the range of 2.5 kHz — 160 kHz leads to a corresponding rise in output voltage from the testing platform. Conversely, when the magnetic field frequency lies between 160 kHz—2 MHz, the output voltage will decrease as the frequency increases. The trend observed is consistent with the experiment result described in Ref.[19], although the type of Hall sensor and test frequency range used in Ref. [21] are different from those in this work. Thus, the platform is capable of accurately assessing the dynamic response characteristics of Hall sensors.

By comparing Fig. 8(a) with Fig. 8(b), it can be observed that there is a significant difference in the amplitude-frequency characteristics of the Hall sensors obtained directly from the testing platform and those calculated using the transfer function. Based on the mathematical relationship between transfer functions, it can be determined that the amplitude-frequency characteristics of the Hall sensors, as shown in Fig. 8(b), indicates an increase in output voltage with increasing frequency when the alternating magnetic field frequency ranges from 2.5 kHz — 280 kHz. However, when the frequency ranges from 280 kHz — 1.5 MHz, there is a decrease in output voltage as the frequency increases. The sensitivities of the three sensor models reach the maximum at 280 kHz, as observed from Fig. 8(b). When the testing frequency is in the range of 2.5 kHz — 38 kHz, the sensitivities of the three Hall sensors are arranged from high to low as NHE520F-8, NHE520F-7 and NHE520F-6. This order is consistent with the order of their sensitivities in a static environment. When the testing frequency is in the range of 38 kHz — 2 MHz, the sensitivities of the three Hall sensors are arranged from high to low as NHE520F-8, NHE520F-6 and NHE520F-7. These results highlight that a more precise amplitude-frequency characteristics of Hall sensors can be obtained by measuring the transfer functions of all the circuit modules and leveraging mathematical relationships between these functions, and the results also prove that the sensitivities of Hall sensors are different in different frequency environments. Therefore, the testing platform can effectively measure the sensitivity of Hall sensor to determine the testing environment of Hall sensor.

The phase-frequency characteristics of the Hall sensor

can be directly measured using the testing platform, as shown in Fig.10. It is observed that when the frequency of the alternating magnetic field is between 2.5 kHz and 16 kHz, the phase of the output voltage of the testing platform lags behind that of the input voltage of the testing platform. However, when the frequency is between 16 kHz and 2 MHz, the phase of the output voltage of the testing platform is ahead of the phase of the input voltage of the testing platform. This trend in phase-frequency characteristics aligns with those reported in Ref.[19] for Hall devices, although there may be differences due to the use of different Hall sensors and tested frequency ranges. Therefore, it can be concluded that this testing platform is capable of measuring the phase-frequency characteristics of Hall sensors. By comparing Fig.10 with Fig.11, it can be observed that there is a significant difference between the phase-frequency characteristics obtained from the testing platform and the phase-frequency characteristics of the Hall sensors. Based on the mathematical relationship between transfer functions, the phase frequency characteristics of Hall sensors NHE520F-6, NHE520F-7 and NHE520F-8 can be obtained, as shown in Fig.11. Within the range of 2.5 kHz—80 kHz, the phase of the output voltage from NHE520F-6 exhibits a lag with respect to the phase of current that generates the alternating magnetic field, whereas within the frequency range of 80 kHz—2 MHz, the phase of output voltage from NHE520F-6 precedes that of current that generates the alternating magnetic field. Within the range of 2.5 kHz—100 kHz, the phase of output voltage from NHE520F-7 exhibits a lag with respect to the phase of current that generates the alternating magnetic field, while within the range of 100 kHz—2 MHz, the phase of output voltage from NHE520F-7 is ahead of the phase of current that generates the alternating magnetic field. Within the range of 2.5 kHz—90 kHz, the phase of output voltage of NHE520F-8 lags behind the phase of current that generates the alternating magnetic field, while within the range of 90 kHz—2 MHz, the phase of output voltage of NHE520F-8 is ahead of the phase of current that generates the alternating magnetic field. These conclusions demonstrate that more accurate phase-frequency characteristics for Hall sensors can be obtained by measuring the transfer function of each circuit module and utilizing mathematical relationships of transfer function of each circuit module.

The study measures the amplitude-frequency and phase-frequency characteristics of the Hall sensor by means of measurement and calculation of transfer functions. However, there is a dearth of research on the dynamic response characteristics of Hall sensor, as well as a lack of established benchmarks for their dynamic response properties. This presents novel avenues for future investigation. Taking the Hall sensor NHE520F as an example, the decrease in Hall voltage with increasing frequency within the range of 280 kHz—2 MHz can be attributed to the influence of alternating magnetic fields on electron movement within the Hall device. As the frequency of the alternating magnetic field exceeds a certain threshold, some electrons are unable to reach both ends where Hall voltage is generated and instead remain confined within the Hall device. The accumulation of these electrons increases with higher frequencies, resulting in a decreasing frequency in Hall voltage within this frequency range. However, further experiments are required to determine the reason for the increase in Hall voltage with increasing frequency when magnetic field frequencies fall between 2.5 kHz—280 kHz, which opens up new avenues for future research. The testing results of the temperature and humidity experiments show that the dynamic response characteristics of the Hall sensor measured by the testing platform will produce disorderly fluctuations with the change of the environment of the testing platform.

Fig.13 and Fig.15 can reflect the difference of data, but they do not find regular changes caused by changes in temperature and humidity, which are more random. The statistical features in Fig.14 and 16 show that the maximum 3σ standard deviation of the amplitude-frequency characteristic of NHE520F does not exceed 37.77% of the mean value, and the maximum 3σ standard deviation of the amplitude-frequency characteristic of P3A does not exceed 22.31% of the mean value in the environment range of 15 ℃—35 ℃ and 50%Rh-70%Rh. The phase frequency characteristics of NHE520F change little with temperature and humidity. When the testing frequency is in the range of 2.5 kHz—10 kHz, the phase frequency characteristics of P3A change little with temperature and humidity, but the test frequency is greater than 10 kHz, and the phase frequency characteristics of P3A fluctuate significantly. According to the statistical knowledge, the probability of the measured values of the dynamic response characteristics of the Hall sensor measured by the testing platform appearing in the region between the positive and negative 3σ deviation is 99.73%. The experimental results show that the 3σ deviation of amplitude-frequency characteristic of Hall sensor NHE520F is less than 15% at low frequency, and the phase-frequency characteristic fluctuation is small. In the range of 100 kHz—1 MHz, the amplitude-frequency

characteristics and phase-frequency characteristics of Hall sensor P3A have obvious deviations in addition to the influence of temperature and humidity, and the influence of system noise on the dynamic characteristics of P3A with the increase of frequency is also a reason that cannot be ignored. Therefore, it can be concluded that under laboratory conditions, the testing results of the platform are effective and can basically reflect the dynamic characteristics of the tested object.

5 Conclusions

The experimental results shows that the dynamic response characteristics of Hall sensors constructed using a linear system approach in this study can yield relatively stable tested results by dynamically updating the transfer functions of the core components. It is also observed that the dynamic characteristic parameters may not necessarily align with the static characteristic parameters. Furthermore, different models of Hall sensors exhibit varying distributions of dynamic characteristics. The experiment indicates that NHE520F-6 offers better cost-effectiveness near the 280 kHz frequency range, while P3A demonstrates higher efficiency towards higher frequency portion.

Acknowledgement

This work was supported by the University Synergy Innovation Program of Anhui Province (No. GXXT-2022-011); The Fundamental Research Funds for the Central Universities (No. JZ2022HGQA0203); And National Natural Science Foundation of China (No. 12075072).

Declaration of conflicting interests

The authors have no conflict of interests related to this publication.

References

[1] ZHANG X, LU S L. Characteristics of new Hall sensor and its application in measurement and control. University Physics, 2002, 21(10): 28.

[2] FAN H, WANG J, FENG Q, et al. Detection techniques of biological and chemical Hall sensors. RSC Advances, 2021, 11(13): 7257-7270.

[3] HU B, CHEN M S, KONG L B, et al. High precision velocity measurement algorithm for small statellite flywheels using linear Hall. Journal of Test and Measurement Technology, 2022, 36(6): 512-517

[4] XIE W C, DAI Y X. A new current measurement method based on Hall Sensor. Chinese Journal of Electronic Measurement and Instrumentation, 2012, 26(8): 705-710.

[5] YOSSI S, BAGRAT K, DIMA C. Towards a low current Hall effect sensor. Sensors and Actuators A: Physical, 2018, 279: 278-283.

[6] HUANG G J, CHEN N M, CHEN K L. Self-calibration method for coreless Hall effect current transformer//2016 IEEE Power and Energy Society General Meeting, July 17-21, 2016, Boston, MA, USA. New York: IEEE, 2016: 1-5.

[7] SHI J D, LIU S, ZHANG L S, et al. Smart textile-integrated microelectronic systems for wearable applications. Advanced Materials, 2020, 32(5): 1901958.

[8] DANIELA D V, BLAGOJEVIC M M, KAYAL M. Microelectronic system for Hall sensor power measurements. Proceedings//2nd IEEE International Workshop on Electronic Design, Test and Applications, January 28-30, 2004, Perth, WA, Australia. New York: IEEE, 2004: 355-359.

[9] WANG A, JI X Q, LIANG S Y, S, et al. Development of bismuth metallic hall sensors for the HL-2A tokamak magnetic measurements. Fusion Engineering and Design, 2024, 199: 114-115.

[10] FERMANDEZ D, HYUN D, PARK Y, et al. Permanent magnet temperature estimation in PM synchronous motors using low-cost hall effect sensors. IEEE Transactions on Industry Applications, 2017, 53(5): 4515-4525.

[11] YU J J, UEDA T. Simultaneous sensing of film thickness and temperature using an InSb Hall element//SPIE Smart Structures and Materials and Nondestructive Evaluation and Health Monitoring, April 20, 2016, Las Vegas, Nevada, USA. Bellingham: SPIE, 2016, 9803: 1158-1164.

[12] TSAI Y P, CHEN K L, CHEN Y R, et al. Multifunctional coreless hall-effect current transformer for the protection and measurement of power systems. IEEE Transactions on Instrumentation and Measurement, 2014, 63(3): 557-565.

[13] ZIEBINSKI A, BREGULLA M, FOJCIK M, et al. Monitoring and controlling speed for an autonomous mobile platform based on the hall sensor//9th International Conference on Computational Collective Intelligence, September 27-29, 2017, Nicosia, Cyprus. 2017: 249-259.

[14] ROY A, SAMPATHKUMAR P, KUMAR P S A. Development of a very high sensitivity magnetic field sensor based on planar Hall effect. Measurement, 2020, 156: 107590.

[15] PABLO N G, Wang G L, GILBERT S C B, et al. Highly compliant planar Hall effect sensor with sub 200 nT sensitivity. npj Flexible Electronics, 2019, 3: 3.

[16] DI MICHELE L, SHELLY C, GALLOP J, et al. Single particle detection: phase control in submicron Hall sensors. Journal of Applied Physics, 2010, 108(10): 103918.

[17] YU Z G, QIN M Y, CHEN X C, et al. Computationally efficient coordinate transformation for field-oriented control using phase shift of linear hall-effect sensor signals. IEEE Transactions on Industrial Electronics, 2019, 67(5): 3442-3451.

[18] ALESSIO D A, EMANUELE B, FRANCESCO S, et al. Uncertainty characterization of a practical system for broadband measurement of battery EIS. IEEE Transactions on Instrumentation and Measurement, 2022, 71(1): 1-9.
[19] SU L M, HAO Q, MA J R. Design of ultra-wideband low noise amplifier based on 0.13 μm CMOS technology. Journal of North University of China(Natural Science Edition), 2013, 34(2): 199-203.
[20] DENG G P, WANG C H. Review on Linearization techniques of ultra-wideband low noise amplifiers. Microelectronics, 2014, 44(1): 85-91.
[21] WANG X Y, YAN Z, JIANG S Qet al. Hall element dynamic characteristic curve of the measurement and study. Journal of college physics, 2017, 4 (3): 52-56.

一种研究线性霍尔传感器频率响应特性的测试平台

刘　宇[1], 胡亮亮[2,3*], 廖明照[4], 周　儒[1], 徐进章[1]

1. 合肥工业大学 电气与自动化工程学院, 安徽 合肥 230009;
2. 合肥工业大学 仪器科学与光电工程学院, 安徽 合肥 230009;
3. 合肥工业大学 测量理论与精密仪器安徽省重点实验室, 安徽 合肥 230009;
4. 合肥工业大学 微电子学院, 安徽 合肥 230601

摘　要： 线性霍尔传感器被广泛用于测量磁场强度，但针对霍尔传感器动态响应特性的研究却很少。为此，设计并搭建了一种线性霍尔传感器的频率响应特性测试平台。该平台由可控恒流源、线圈、线性霍尔传感器、低噪声放大器和数据采集装置组成，通过构建系统传递函数并提出动态更新的传递函数的方法，实现了霍尔传感器动态响应特性的精确测量。利用该平台分别测试了NHE520F和P3A两款芯片的动态特性性能。结果显示，在2.5 kHz－2 MHz范围内，这两款霍尔传感器在幅频特性和相频特性方面的性能差异在测试平台上被充分显现，而且霍尔传感器的动态特性参数与静态特性参数并非必然一致，动态特性分布也不相同。此外，根据多种温湿度条件下测得的霍尔传感器幅频特性与相频特性，绘制了霍尔传感器的平均动态特性曲线和3个标准差包络曲线。基于该测试平台获得的实验数据对研究霍尔传感器动态响应特性具有重要意义。

关键词： 霍尔传感器；磁场测量；幅频特性；相频特性

引用格式： LIU Yu, HU Liangliang, LIAO Mingzhao, et al. A testing platform for frequency response characteristics of linear Hall sensors. Journal of Measurement Science and Instrumentation, 2024, 15(1): 105-119.